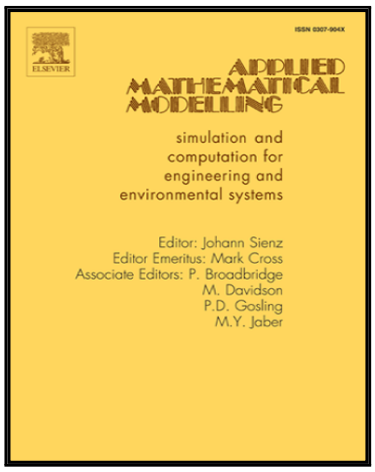


# On implicit integration of the bounding surface model based on swell–shrink rules

Jian LI

PII: S0307-904X(16)30264-5
DOI: 10.1016/j.apm.2016.05.014
Reference: APM 11167

To appear in: *Applied Mathematical Modelling*

Received date: 17 January 2015
Revised date: 11 May 2016
Accepted date: 18 May 2016

Please cite this article as: Jian LI , On implicit integration of the bounding surface model based on swell–shrink rules, *Applied Mathematical Modelling* (2016), doi: 10.1016/j.apm.2016.05.014

**Highlights**

- A modified dynamic constitutive model that can better describe the soil elastoplastic deformation behavior is introduced.
- A specific application of the return mapping algorithms is introduced in this paper.
- There are many necessary modifications of the return mapping algorithms which must be of interest to the readership.

# On implicit integration of the bounding surface model based on swell–shrink rules

Corresponding author: Jian LI, PhD, Assistant Researcher
State Key Laboratory of Geomechanics and Geotechnical Engineering, Institute of Rock and Soil Mechanics, Chinese Academy of Sciences, Xiaohongshan, Wuchang, Wuhan 430071, Hubei, P. R. China
E-mail: lij@whrsm.ac.cn

**ABSTRACT**
The bounding surface model has become one of the most widely used constitutive models for representing the elastoplastic behavior of soils under cyclic loads. Using a bounding surface model modified to include swell–shrink rules, this paper gives a full description of a popular return mapping algorithm based on implicit integration. The algorithm allows complete implicit integration and consistent linearization of the model to be achieved. Several modifications are made to force the algorithm to satisfy the computational needs of the model and a Newton–Simpson iterative method is introduced to ensure high numerical accuracy. Numerical simulations are used to demonstrate the validity of the algorithm presented.

**Keywords:** implicit integration; return mapping algorithm; Newton–Simpson iterative method; modified bounding surface model; swell–shrink rules

## 1. Introduction

A large number of cyclic triaxial tests indicate that the relationship between the stress and strain of soil subjected to cyclic loads appears to show nonlinearity and hysteresis characteristics which reflects the elastoplasticity of the soil under cyclic load (Kaynia, Madshus, & Zackrisson, 2000; Wang, 2007; Yang, Wang, & Luan, 2010; Wei, Liu, & Gao, 2007; Hu, Liu, & Huang, 2012). A proper constitutive model should correctly represent these characteristics and accurately describe the hysteresis between the stress and strain in the soil. Attempts to realize this has led to the development of several major categories of cyclic constitutive models, e.g. the multi-surface elastoplastic model (Mroz, Norris, & Zienkiewicz, 1978; Mroz, Norris, & Zienkiewicz, 1979; Prevest, 1977; Wang & Yao, 1996; Xu, Xie, & Zheng, 1995), endochronic elastoplastic model (Bazant & Bhat, 1976; Bazant, Ansal, & Krizek, 1979; Zienkiewicz, Chang, & Hinton, 1978), transient limit equilibrium theory (Xie, Wu, & Guo, 1981; Xie, Wu, & Guo, 1981; Xie & Zhang, 1987), bounding surface elastoplastic model (Dafalias, 1986; Manzari & Dafalias, 1997; Dafalias, 1986; Dafalias, 1987), etc.

Among the numerous cyclic constitutive models, the bounding surface model is the most popular due to its comparatively theoretical simplicity and relatively low requirement for complex arithmetic (Manzari & Nour, 1997; Ronaldo, Borja, & Lin etc., 2001). In this paper, a modified bounding surface model is introduced based on ‘swell–shrink’ rules. The model describes the characteristics of clay under cyclic loads very well and also has a simple theoretical form which only requires a simple integration algorithm.

When describing the mechanical characteristics of soil, a strategy involving numerical integration is needed throughout the whole loading process. In recent years, a number of often robust and accurate algorithms referred to as ‘return mapping algorithms’ have been widely

implemented which include both explicit and implicit integration (Manzari & Nour, 1997; Ronaldo, Borja, & Lin etc., 2001; Ortiz & Simo, 1986; Simo & Govindjee, 1991; Simo, 1985). Due to their high accuracy, however, backward Euler schemes involving implicit integration are often used in practice. In spite of their widespread use in classical elastoplastic constitutive models, return mapping algorithms based on implicit backward schemes still have to be modified to fit the computational needs of the bounding surface model. This is mainly due to the characteristics of the model itself. For example, in bounding surface models all the stress points are enveloped in the bounding surface and a consistency condition needs to be applied (according to the bounding surface equation) due to the lack of a yield surface (upon which the return mapping algorithm is usually performed). In the modified bounding surface model presented in this paper, new swell–shrink rules are added to the algorithm.

Based on a previously-proposed modified bounding surface model (Li, 2013), this paper presents the complete deduction process involved in the integration model (the detailed algorithm itself is given in Appendix A). A key feature of the process of combining the return mapping algorithm with the modified bounding surface model is that an iterative Newton–Simpson method can be invoked when deducing the control equation group. This guarantees high accuracy and efficiency. In addition, during the process of computation, the stress point is always kept on the bounding surface throughout the elastic loading or unloading phases. This forces the algorithm to represent the elastoplastic characteristics of the soil. The algorithm presented was embedded into the FLAC3D package and several validation tests performed to verify the precision and efficiency of the model and algorithm used. As a general aid to the reader, all the symbols used in this paper are listed in Appendix B.

## 2. Modified bounding surface model based on swell–shrink rules

Daliafas and Herman proposed a constitutive model called the ‘bounding surface model’ in 1986 based on the Cam-clay model. The model was able to stimulate the stress–strain relationship in soil under cyclic loading conditions and overcome the difficulties caused by tracing the multiple nested yield surfaces and their movement. However, the bounding surface model considers the unloading and reloading phases in the elastic region, and so it cannot, therefore, reflect the nonlinear stress–strain relationship in the two phases. As a result, the bounding surface model must be subsequently modified (Liang & Ma, 1992; Zhou, Sun, & Wu, 2002; Anadarajah & Dafalias, 1986).

For the reasons outlined above, a modified bounding surface model based on swell–shrink rules has been proposed (Li, 2013). The modified model is based on critical state theory and bounding surface plasticity. In the calculations performed, the bounding surface does not need to be predefined. Instead, it is taken to be the biggest yield surface formed in the initial loading phase (this overcomes the defect that the bounding surface need to be predefined in the model application phase). It also simplifies parameter calibration and makes the model more convenient to apply. Only the main aspects of the theory are discussed here — a more detailed account can be found in the paper by Li (2013).

The modified bounding surface model based on swell–shrink rules consists mainly of: (1) a bounding surface equation; (2) a mapping rule; (3) the plastic flow and swell–shrink rules; and (4) computation of the plastic modulus. We discuss these features in turn.

### 2.1 Bounding surface equation

The specific bounding surface equation used here has the form (Li, 2013; Chen, Li, & Jiang, 2013):

$$F = Q = \bar{s}_{ij}\,\bar{s}_{ij} + \frac{2}{3}[M^{'}(\bar{p},\theta_{\sigma})]^2\,\bar{p}(\bar{p}-\bar{p}_c) \tag{1}$$

$$M^{'}(\bar{p},\theta_{\sigma}) = \frac{2mM_c}{(1+m)-(1-m)\sin 3\theta_{\sigma}}\frac{1}{ap+b} \tag{2}$$

where $m = \frac{M_e}{M_c}$ , $0.7 \leqslant m \leqslant 1.0$; $M_e = \frac{q_e}{p_e}$ ; $M_c = \frac{q_c}{p_c}$ ; and $-\frac{\pi}{6} \le \theta_{\sigma} = \frac{1}{3}\sin^{-1}\left[\frac{3\sqrt{3}J_3}{2J_2^{3/2}}\right] \le \frac{\pi}{6}$.

From Eqs. (1) and (2), it can be seen that the above equation for the bounding surface takes the nonlinear critical state into account, which means that the critical state line(CSL) in the p-q stress space is a hyperbolic curve($M_c$ and $M_e$ shown in Fig. 1). Besides, the S-D effect which indicates that the compression strength is bigger than the extension strength is also considered. An illustration of its shape is shown in Fig. 1.

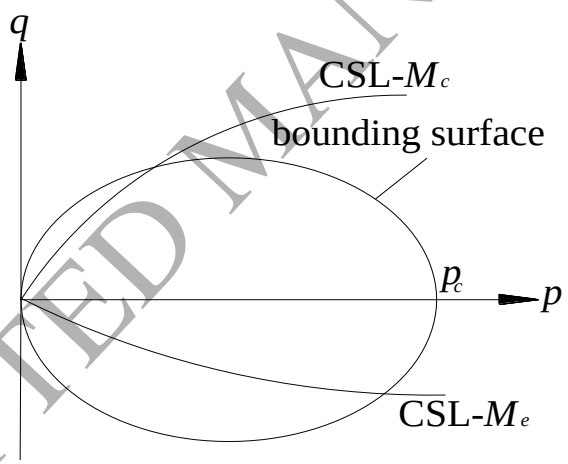


**Fig. 1.** The modified bounding surface.

**2.2 Mapping rule**

For soil, the elastic area is considered to be non-existent in stress space. Therefore, the mapping origin can be fixed at the coordinate origin. The mapping rule is shown in Fig. 2 and can be expressed in the form:

$$\bar{\sigma}_{ij} = c\sigma_{ij} \quad , \quad c = \frac{\delta_0}{\delta_0 - \delta} \tag{3}$$

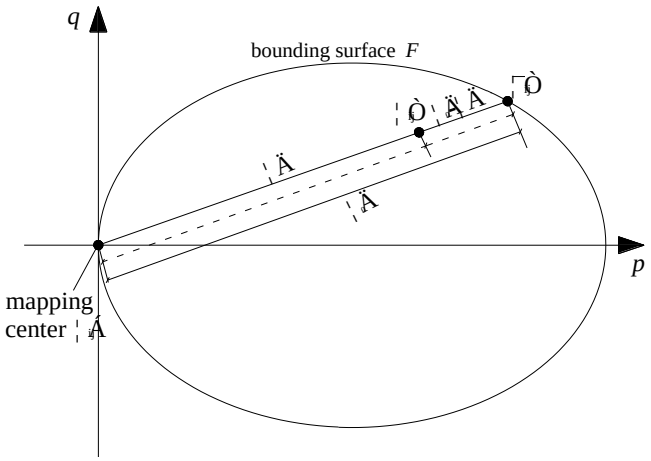


**Fig. 2.** The mapping rule

### 2.3 Plastic flow and bounding surface swell–shrink rules

#### *2.3.1 Plastic flow rules*

An associated flow rule is used here, as shown in Eqs. (4) and (5):

$$\dot{\varepsilon}_{ij}^{p} = \lambda \frac{\partial F}{\partial \bar{\sigma}_{ij}} \tag{4}$$

$$\dot{p}_c = p_c \frac{v}{\lambda - \kappa} \dot{\varepsilon}_v^p \tag{5}$$

#### *2.3.2 Swell–shrink rules of the bounding surface*

Several bounding surface swell–shrink rules are proposed. Whenever we are in the loading or unloading stages, there must be a 'virtual stress' $\bar{\sigma}_{ij}$' which is obtained from the mapping rule in accordance with the stress state in a new stress step. This virtual stress ' is substituted into the bounding surface equation $F$ to judge whether the virtual stress state exceeds $F$ or not. When $F > 0$ the virtual stress exceeds the bounding surface equation and the bounding surface swells according to the hardening rules. When $F > 0$ the virtual stress is within the bounding surface and the bounding surface shrinks to make sure the virtual stress lies on $F$. However, there is no plastic strain produced in this stress step. The swell–shrink rules can be expressed as shown in Fig. 3.

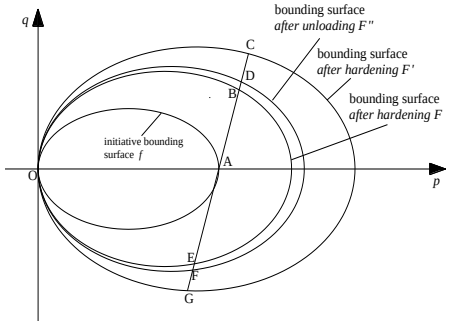


**Fig. 3.** The swell–shrink rules of the bounding surface.

In Fig. 3, it can be seen that the stress path is a→b→c→d→e→f→g. In the loading process

from isotropic consolidation stress point a to b, the initial bounding surface *f* swells to *F* along with development of plastic strain. If loading is continued to stress point c, the bounding surface swells to *F'*. After that, in the unloading process from c to d, if there is no change to the plastic strain, then the bounding surface shrinks to *F"* to make the stress point lie on the bounding surface. After unloading to a, if loaded to e, the bounding surface swells to *F* along with elastoplasticity development. If reverse loading is continued to g, then the bounding surface swells to *F'*.

### 2.4 Solving for the plastic modulus

One key aspect of the bounding surface model is the method used to compute the plastic modulus. According to theory, the plastic modulus can be found using interpolation. The relationship between $K_p$ and $\bar{K}_p$ is determined by the stress tensor $\sigma_{ij}$, the inner variable $q_n$, and the distances $\delta, \delta_0$ between the stress points. Here, the interpolation function proposed by Manzari is used (Manzari & Nour, 1997) which has the form:

$$K_p = \bar{K}_p + H_0 \frac{16M^4\nu}{9(\lambda-\kappa)} \bar{p}^3 \left(\frac{c-1}{c}\right) \tag{6}$$

## 3. Return mapping algorithm

A good constitutive model algorithm should be convenient to implement, satisfy the incremental plastic consistency requirement, and have good accuracy and stability (Krieg, 1977; Schreyer, Kulak, & Kramer, 1979; Ortiz & Popov, 1985). From this standpoint, a number of authors have proposed the so-called 'return mapping algorithm' for the integration of elastoplastic constitutive model equations. In this section, the main features of such algorithms are discussed to show how the procedure works.

The return mapping process is illustrated in Fig. 4. From Fig. 4 it can be seen that the return mapping algorithm has two main procedures: elastic prediction (path I in the figure) and plastic correction (path II). Note that the plastic correction process is carried out in a step-by-step fashion. Furthermore, the direction involved in the correction step, $R_{ij}$, is controlled by the yield function *F* and follows the steepest descent path corresponding to *F* — the direction is computed from the elastic modulus.

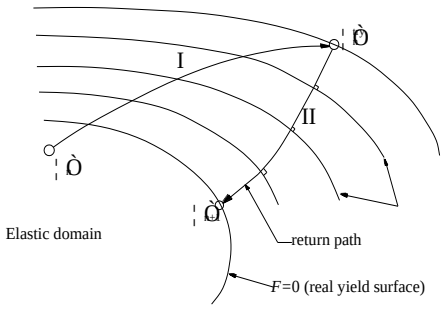


**Fig. 4.** Scheme illustrating the return mapping algorithm.

These characteristics can be deduced as follows. For $\sigma_{n+1}$, we have:

$$\sigma_{n+1} = \sigma_n + E\left(\dot{\varepsilon}_{ij}^{try} - \dot{\varepsilon}_{ij}^{p}\right) \tag{7}$$

For $\dot{\varepsilon}_{ij}^{p}$, we have:

$$\dot{\varepsilon}_{ij}^{p} = \dot{L} R_{ij} \tag{8}$$

where, $R_{ij} = \dfrac{\partial F}{\partial \sigma_{ij}}$.

As a result, the stress plastic corrector is:

$$\dot{\sigma}_{ij}^{p} = E\dot{\varepsilon}_{ij}^{p} = E\dot{L}R_{ij} = E\dot{L}\frac{\partial F}{\partial \sigma_{ij}} \tag{9}$$

Dividing Eq. (7) throughout by $\langle \dot{L} \rangle$, produces:

$$\frac{\dot{\sigma}_{ij}^{p}}{\dot{L}} = E\frac{\partial F}{\partial \sigma_{ij}} \tag{10}$$

Eq. (10) can be used to determine the direction of the plastic correction needed in each step of the correction process. It also proves one of the characteristics of the return mapping algorithm discussed later.

There are generally two main methods used to conduct plastic correction which involve explicit and implicit methods of iteration. For high accuracy and stability, an implicit iterative method is preferred and is the solution method adopted here. The whole algorithm, and the procedures therein, are illustrated in Table 1.

**Table 1** The return mapping algorithm

| | | |
|---|---|---|
| (i) Elastic prediction: | $\dot{\varepsilon}_{n+1}^{(0)} = \dot{\varepsilon}_{n+1}^{e(0)} = \dot{\varepsilon}_{n+1}^{try}$<br>$\dot{\varepsilon}_{n+1}^{p(0)} = 0$<br>$\sigma_{n+1}^{(0)} = \sigma_{n}^{(0)} + E\dot{\varepsilon}_{n+1}^{try}$<br>$q_{n+1}^{(0)} = q_{n}^{(0)}$ | |
| (ii) Check for yield: | $F(\sigma_{n+1}^{(0)}, q_{n+1}^{(0)}) > 0$? | |
| Yes: | | Goto (iii) |
| No: | $\dot{\varepsilon}_{n+1} = \dot{\varepsilon}_{n+1}^{\text{try}}$, $\dot{\varepsilon}_{n+1}^{p} = \dot{\varepsilon}_{n+1}^{p(0)} = 0$, $\sigma_{n+1} = \sigma_{n+1}^{(0)}$, $q_{n+1} = q_{n+1}^{(0)}$ | Goto (v) |
| (iii) Plastic correction: | | |
| Implicit iterative method: | $f^{(i)} = \begin{cases} \sigma_{n+1}^{(i)} = \sigma_{n} + E(\dot{\varepsilon}_{n+1}^{try} - \dot{\varepsilon}_{n+1}^{p(i)}) \\ \dot{\varepsilon}_{n+1}^{p(i)} = \langle L \rangle R_{ij}^{(i)} \\ \dot{q}_{n+1}^{(i)} = \langle L \rangle r_{n}^{(i)} \\ F^{(i)} = 0 \end{cases}$ | |
| (iv) Convergence check: | | |
| | $\left\| f^{(i)} \right\| < TOL$? | |
| Yes: | $\dot{\varepsilon}_{n+1}^{p} = \dot{\varepsilon}_{n+1}^{p(i)}$, $\dot{\varepsilon}_{n+1} = \dot{\varepsilon}_{n+1}^{\text{try}} - \dot{\varepsilon}_{n+1}^{p(i)}$, $\sigma_{n+1} = \sigma_{n+1}^{(i)}$, $q_{n+1} = q_{n+1}^{(i)}$ | Goto (v) |
| No: | $i \to i+1$ | Goto(iv) |
| (v)Stress update: | | |
| | $\sigma_{n+1} = \sigma_{n} + E(\dot{\varepsilon}_{n+1}^{try} - \dot{\varepsilon}_{n+1}^{p})$ | Next increment step |

## 4. Implicit integration for the model

### 4.1 Incremental constitutive relationships

Corresponding to the modified bounding surface model, the incremental constitutive relationships are derived as follows.

(1) *Elastic strain*

By decomposing the volumetric and deviatoric parts of the strain tensor we obtain:

$$\dot{p} = K\dot{\varepsilon}_v^e = K\left(\dot{\varepsilon}_v - \dot{\varepsilon}_v^p\right) \tag{11}$$

$$\dot{s}_{ij} = 2G\dot{e}_{ij}^e = 2G\left(\dot{e}_{ij} - \dot{e}_{ij}^p\right) \tag{12}$$

Due to the extension from critical state theory and bounding surface model, the bulk and shear moduli are functions of the current stress state and some other parameters (referred to as 'hyperelasticity'). Expressions for these quantities are given by:

$$K = \frac{v}{\kappa} p \tag{13}$$

$$G = \frac{3(1-2\mu)}{2(1+\mu)} K \tag{14}$$

Note that $v$ is the current specific volume, which means that it will vary with deformation of the soil. Its change can be calculated using $\dot{v}/v = -\dot{\varepsilon}_v$.

(2) *Flow and hardening rules*

According to the theory, the flow rule can be expressed in the form:

$$\dot{\varepsilon}_v^p = L\frac{\partial F}{\partial \bar{p}}; \quad \dot{e}_{ij}^p = L\frac{\partial F}{\partial \bar{s}_{ij}} \tag{15}$$

To calculate the plastic strain increments $\dot{\varepsilon}_v^p$ and $\dot{e}_{ij}^p$, the plastic multiplier $L$ must first be determined. $L$ can be computed using the following equation:

$$L = \frac{1}{K_p}\left(\frac{\partial F}{\partial \bar{s}_{ij}}\dot{s}_{ij} + \frac{\partial F}{\partial \bar{p}}\dot{p}\right) = \frac{1}{\bar{K}_p}\left(\frac{\partial F}{\partial \bar{s}_{ij}}\dot{\bar{s}}_{ij} + \frac{\partial F}{\partial \bar{p}}\dot{\bar{p}}\right) \tag{16}$$

An isotropic hardening law is used to characterize the evolution of the bounding surface with the change in void ratio:

$$\dot{\bar{p}}_c = \bar{p}_c \frac{v}{\lambda - \kappa}\dot{\varepsilon}_v^p \tag{17}$$

(3) *Plastic modulus*

The plastic modulus $K_p$ can be obtained from Eq. (6). However, the value of the virtual plastic modulus $\bar{K}_p$ must be confirmed. $\bar{K}_p$ can be calculated from the consistency condition, as follows:

$$\dot{F} = \frac{\partial F}{\partial \bar{s}_{ij}}\dot{\bar{s}}_{ij} + \frac{\partial F}{\partial \bar{p}}\dot{\bar{p}} + \frac{\partial F}{\partial \bar{p}_c}\dot{\bar{p}}_c = 0 \tag{18}$$

Thus, $\bar{K}_p$ is such that:

$$\bar{K}_p = -\frac{\partial F}{\partial \bar{p}_c}\bar{p}_c\frac{v}{\lambda-\kappa}\frac{\partial F}{\partial \bar{p}} \tag{19}$$

(4) *Other relationships*

Several complementary equations are required to finish off the set of model relationships:

$$\begin{cases}\dfrac{\partial F}{\partial \bar{p}} = [M^{'}(\theta_\sigma)]^2(2\bar{p}-\bar{p}_c)\\ \dfrac{\partial F}{\partial \bar{s}_{ij}} = 3\bar{s}_{ij}\\ \dfrac{\partial F}{\partial \bar{p}_c} = -[M^{'}(\theta_\sigma)]^2\bar{p}\end{cases} \tag{20}$$

Overall, the complete set of incremental constitutive relationships have now been expressed and by combining Eqs. (1), (3), and (6) the stress–strain curve can be calculated by substituting the expressions in Eq. (20) into the incremental relations.

**4.2 Implicit integration based on the return mapping algorithm**

As already discussed, the implicit integration scheme based on the return mapping algorithm has, generally speaking, three integration procedures which involve an elastic prediction phase, a state judgment phase, and a plastic correction phase. First, at the beginning of each strain increment, an elastic response is assumed and the corresponding stress is calculated. Second, the estimated stress and strain are substituted into the bounding surface equation to test the state of the bounding surface equation. Finally, some corrections are made according to the state of the bounding surface equation, and the bounding surface is allowed to swell or shrink. The details of this procedure are discussed in this section.

(1) *Elastic prediction phase*

According to the elastic prediction, we have:

$$p^{n+1} = p^n + K^{n+1}\Delta\varepsilon_v \tag{21}$$

$$s_{ij}^{n+1} = s_{ij}^n + 2G^{n+1}\Delta e_{ij} \tag{22}$$

where the superscripts $n$ and $n$+1 represent the current time and the next time increment, $\Delta\varepsilon_v$ is the estimated elastic volumetric strain increment, and $\Delta e_{ij}$ is the deviatoric strain increment.

Note that $K^{n+1}$ and $G^{n+1}$ are related to current parameters and can be calculated using:

$$K^{n+1} = \frac{v^n}{\kappa}p^n \tag{23}$$

$$G^{n+1} = \frac{3(1-2\mu)}{2(1+\mu)}K^{n+1} \tag{24}$$

(2) *State judgment phase*

In this phase, $c^n$ (the algorithm for which will be discussed later), $p^{n+1}$, and $s_{ij}^{n+1}$ need to be put into the bounding surface expression in Eq. (1) to judge the state of the bounding surface equation.

If $F(c^n p^{n+1}, c^n s_{ij}^{n+1}) > 0$, a correction must be made to force the estimated stress and strain to satisfy the plastic equation and the bounding surface swells. However, if $F(c^n p^{n+1}, c^n s_{ij}^{n+1}) < 0$, the bounding surface will shrink. In a word, no matter which state the bounding surface equation is in, the virtual stress must be on the bounding surface curve.

(3) *Plastic correction phase* (*when* $F(c^n p^{n+1}, c^n s_{ij}^{n+1}) > 0$)

The purpose of performing plastic correction based on flow and hardening rules is to force the stress state to satisfy the consistency condition. In other words, it is to keep the stress state on the bounding surface curve.

Plastic correction is the key part of the whole integration procedure. In this phase, the equations for plastic strain, corrected stress, hardening parameter, bounding surface condition, and plastic modulus constitute an integral iterative equation group which can be solved by applying an iterative Newton–Simpson method.

(1) *Plastic strain equations*

According to the expressions in Eq. (15), the integration formula can be expressed in the form:

$$\begin{cases} \left(\Delta\varepsilon_v^p\right)^{n+1} = L^{n+1}\dfrac{2}{3}M^2\left(2c^{n+1}p^{n+1} - p_c^{n+1}\right) \\ \left(\Delta e_{ij}^p\right)^{n+1} = 2L^{n+1}c^{n+1}s_{ij}^{n+1} \end{cases} \tag{25}$$

(2) *Hardening parameter equation*

The hardening parameter $p_c$ can be computed by applying the backward Euler integration algorithm:

$$p_c^{n+1} = p_c^n \exp\left(\frac{v^n}{\lambda-\kappa}\left(\Delta\varepsilon_v^p\right)^{n+1}\right) \tag{26}$$

(3) *Bounding surface control equation*

The corrected virtual stress must stay on the bounding surface equation

$$F = c^{n+1}s_{ij}^{n+1}c^{n+1}s_{ij}^{n+1} + \frac{2}{3}M^2c^{n+1}p^{n+1}\left(c^{n+1}p^{n+1} - p_c^{n+1}\right) = 0 \tag{27}$$

(4) *Stress correction*

According to Eqs. (11) and (12), the stress can be corrected using the expressions:

$$\begin{cases} p^{n+1} = p^n + K\left(\left(\Delta\varepsilon_{\mathrm{v}}\right)^{n+1} - \left(\Delta\varepsilon_v^p\right)^{n+1}\right) \\ s_{ij}^{n+1} = s_{ij}^n + 2G\left(\left(\Delta e_{ij}\right)^{n+1} - \left(\Delta e_{ij}^p\right)^{n+1}\right) \end{cases} \tag{28}$$

At this stage, we note that there are presently 16 equations in the iterative equation group and 17 unknowns ($\Delta\varepsilon_v^p$, $6\Delta e_{ij}^p$, $p_c$, $p$, $6s_{ij}$, $c$, $L$). Therefore, there needs to be another control equation. In the equation group, we see that there is a parameter $c^{n+1}$ which does not have its own control equation.

(5) *Control equation for* $c^{n+1}$

An equation for $c^{n+1}$ can be obtained by substituting into Eq. (16) the differential relationship

between the virtual stress $\bar{\sigma}_{ij}$ and the real stress $\sigma_{ij}$.

The differential relationship between $\bar{\sigma}_{ij}$ and $\sigma_{ij}$ is derived from Eq. (3):

$$\begin{cases} \mathrm{d}\bar{p} = p\mathrm{d}b + b\mathrm{d}p \\ \mathrm{d}\bar{s}_{ij} = s_{ij}\mathrm{d}b + b\mathrm{d}s_{ij} \end{cases} \tag{29}$$

Substituting Eq. (29) into Eq. (16) and then rearranging, we have:

$$\mathrm{d}c = L\frac{\bar{K}_p - cK_p}{\frac{2}{3}M^2 pp_c} \tag{30}$$

Substituting $L = \frac{1}{\bar{K}_p}\frac{2}{3}M^2 cpp_c$ into this we get:

$$\mathrm{d}c = c\left(1 - c\frac{K_p}{\bar{K}_p}\right)\frac{\mathrm{d}p_c}{p_c} \tag{31}$$

Using backward Euler integration, we have:

$$c^{n+1} = -\frac{XY}{c^n - k_p^{n+1} - c^n p_c^{n+1}/p_c^n} \tag{32}$$

where $XY = \frac{c^n k_p^{n+1} p_c^{n+1}}{p_c^n}$, $k_p = \frac{\bar{K}_p}{K_p}$.

Here, we have a new unknown $k_p$ and therefore another control equation must be found.

(6) *Control equation for $k_p$*

From Eqs. (6), (17), and (18), we find:

$$k_p^{n+1} = \frac{\bar{K}_p}{K_p} = \frac{\mathrm{XX}}{\mathrm{XX} + 4\mathrm{H}_0 c^{n+1}\left(c^{n+1} - 1\right)} \tag{33}$$

where $\mathrm{XX} = \left(2c^{n+1} - p_c^{n+1}/p^{n+1}\right)p_c^{n+1}/p^{n+1}$.

Now there are 18 equations and 18 unknowns. Therefore, all the unknowns can be calculated using the Newton–Simpson iterative method.

Up to this point, the incremental stress and strain tensors at moment $n$ may be obtained provided $F(c^n p^{n+1}, c^n s_{ij}^{n+1}) > 0$. When $F(c^n p^{n+1}, c^n s_{ij}^{n+1}) < 0$, the bounding surface must shrink according to the theory and the relevant control equation is:

$$\bar{p}_c = \frac{\bar{s}_{ij}\bar{s}_{ij}}{\frac{2}{3}M(\theta_\alpha)^2\bar{p}} + \bar{p} \tag{34}$$

Details of the algorithm for implementing the implicit integrations mentioned in this section are given in Appendix A.

## 5. Model validation

The modified bounding surface model discussed here was implemented in FLAC3D according to the proposed implicit integration method based on the return mapping algorithm. Conventional and cyclic load triaxial tests on clay samples were simulated (the clay soil specimens had compactness values of 0.8, 0.85, and 0.95). By comparing the calculated stress–strain relationships with data from real tests, the model and its algorithm could be verified. The strength parameters (*a* and *b*) and other parameters for the model are shown in Tables 2 and 3, respectively.

**Table 2** The strength parameters of the critical state line of the soil.

| Compactness | *a* | *b* |
|---|---|---|
| 0.80 | 0.0009 | 0.6874 |
| 0.85 | 0.0008 | 0.3581 |
| 0.95 | 0.0007 | 0.2843 |

**Table 3** Parameter values for the present model.

| Compactness | Initial specific volume, $v$ | Compression index, $\lambda$ | Swelling index, $\kappa$ | Bulk modulus, $K$ (MPa) | Poisson ratio, $\mu$ | $H_0$ |
|---|---|---|---|---|---|---|
| 0.80 | 2.21 | 0.19 | 0.026 | 16.7 | 0.3 | 20 |
| 0.85 | 1.92 | 0.15 | 0.018 | 33.3 | 0.28 | 20 |
| 0.95 | 1.43 | 0.13 | 0.014 | 60.2 | 0.26 | 20 |

### 5.1 Conventional triaxial tests

Figures 5–7 show the results of the conventional triaxial calculations on clay samples with different compactness values.

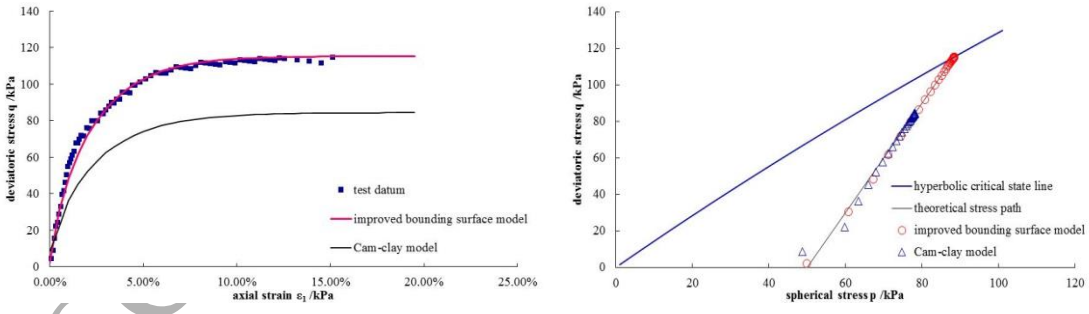


(a) Stress–strain curve (b) Stress path

**Fig. 5.** Comparison of the results of the numerical simulations and real test data for a compactness value of 0.80.

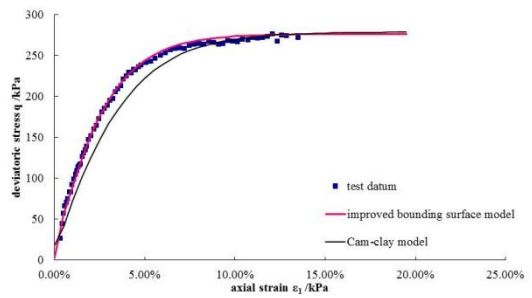


(a) Confining pressure 50 kPa

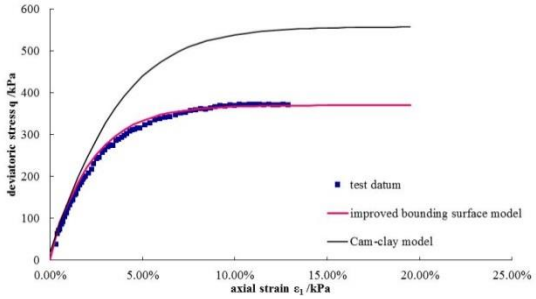


(b) Confining pressure 100 kPa

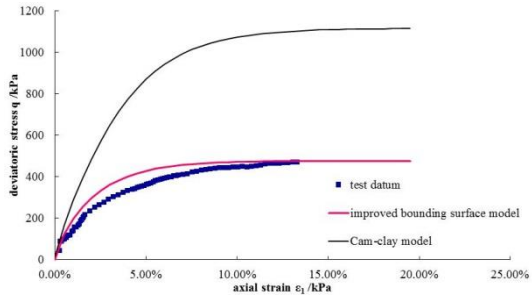


(c) Confining pressure 200 kPa

**Fig. 6.** Comparison of the results of the numerical simulations and real test data for a compactness value of 0.85.

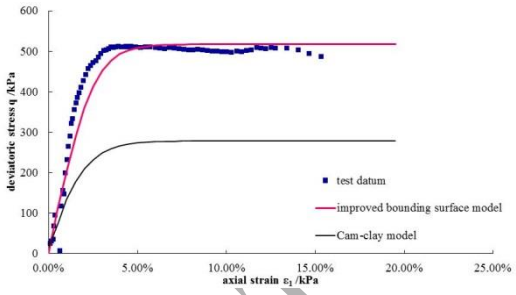


(a) Confining pressure 50 kPa

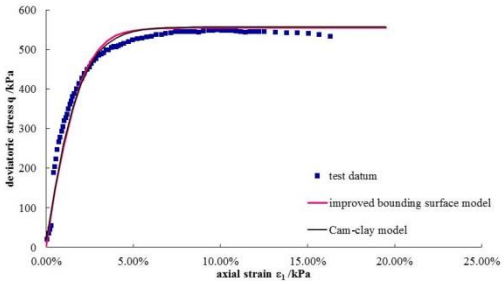


(b) Confining pressure 100 kPa

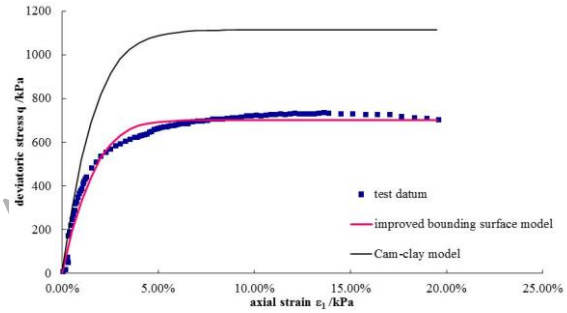


(c) Confining pressure 200 kPa

**Fig. 7.** Comparison of the results of the numerical simulations and real test data for a compactness value of 0.95.

From Figs. 5(a), 6, and 7, it can be seen that the modified model can simulate the nonlinearity of the stress–strain relationship in the clay samples and the plastic flow characteristics very well.

Fig. 5b also shows that the stress path calculated using the present constitutive model matches the theoretical stress path and reaches the hyperbolic critical line. However, the stress path computed by the well-known Cam-clay model is shorter that the theoretical stress path (due to the small value of *M* involved).

From Figs. 6 and 7, it can be seen that although it is possible to simulate the mechanical characteristics well by adjusting the value of *M* to make the critical line pass through the critical state of the stiff clay for a given confining pressure, the Cam-clay model cannot give good simulation results when the confining pressure is changed. This is because the linear critical line in the Cam-clay model is not capable of comprehensively describing the critical state of the stiff clay. For example, in Fig. 6 the Cam-clay model simulates the mechanical features of the clay sample well under a confining pressure of 50 kPa if the value of *M* is adjusted, however, the calculation results are unsatisfactory for the other two higher confining pressures. This is because the strength under a small confining pressure is greater (relatively). However, if the confining pressure increases then the range of the strength increase is reduced. At this point, continuing to use a linear critical line causes the predicted strength to be greater than that of real stiff clay (as can be seen in Figs. 6(b) and 6(c)). From Fig. 7, the same conclusion can be made. Nevertheless, the modified bounding surface model overcomes this defect and continues to simulate the mechanical characteristics of the stiff clay very well.

### 5.2 Cyclic load triaxial tests

Figures 8 and 9 show the cyclic load triaxial calculation results for clay samples with a compactness of 0.8 and consolidation ratio of 3.0.

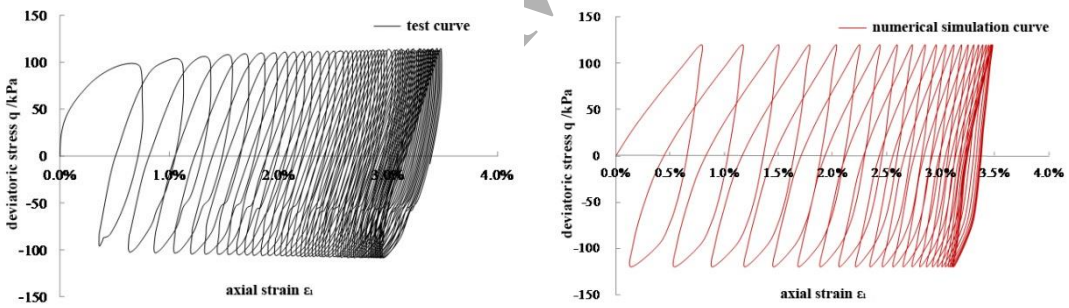


(a) test curve (b) numerical simulation curve

**Fig. 8.** Comparison of a simulated stress–strain curve for soil subjected to cyclic loading and that obtained from real tests ( $\sigma_d$ = 120 kPa).

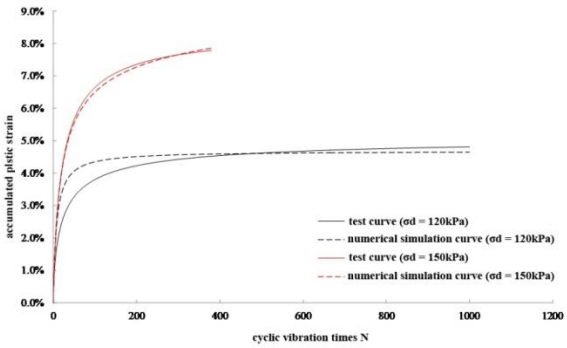

**Fig. 9.** Comparison of simulated results for accumulated plastic strain under cyclic loading with real test results.

From Figs. 8 and 9, it can be seen that the curves calculated using the numerical simulation method match well the curves obtained in real tests. In Fig. 9, the calculated accumulated plastic strain appears to develop slightly faster than in the real tests when the cyclic stress amplitude is small. Nevertheless, the accumulated strain becomes steady later on and the difference between the numerical simulations and test results is small. If the cyclic stress is high, the two curves match each other very well (although the final value of the accumulated plastic strain is a little larger than the actual measured value).

Overall, the calculation results show that the cyclic constitutive model and the implicit algorithm proposed in this paper can describe cyclic stress–strain relationships and trends in plastic strain development in clay subjected to cyclic loading very well. In addition, the numerical calculation results are stable and the computational efficiency is high.

## 6. Conclusions

In this paper, a modified bounding surface constitutive model based on swell–shrink rules has been briefly introduced for clay. In addition, a detailed account of the full implicit integration algorithm has been given. One of the key features of the implicit integration process is the use of a return mapping algorithm, which ensures the method has high accuracy and stability. Because of the plastic correction and bounding surface shrink algorithm, the model can accurately reflect the elastoplastic characteristics of the clay under cyclic loads, particularly in the unloading and reloading stages.

To aid implementation, incremental constitutive relationships for the modified bounding surface model have been given and the corresponding implicit integration (based on the return mapping algorithm) has been presented in detail. The model was developed using the FLAC3D package and several validation tests were completed. The results of the validation studies show that the model can simulate the mechanical characteristics of the clay pretty well and that the corresponding algorithm is stable and accurate.

## References


Kaynia M A, Madshus C, Zackrisson P. (2000). Ground vibration from high-speed trains: prediction and countermeasure. *ASCE Journal of Geotechnical and Geoenviromental Engineering, 126(6)*, 531-537.

Wang J. (2007). Study on dynamic behavior of saturated soft clay under unidirectional and bidirectional cyclic loading. Hangzhou: Zhejiang University.

Yang Q, Wang M, Luan MT etc. (2010). Experimental research of correlation on static and dynamic strength of unsaturated silty clay. *Rock and Soil Mechanics, 31(01)*, 71-80.

Wei H. B., Liu H. B., Gao Y. P. etc. (2007). Experimental research on dynamic properties of fly ash soil subjected to freeze-thaw cycles. *Rock and Soil Mechanics, 28(5)*, 1005-1008.

Hu C, Liu H. X., Huang W. (2012). Anisotropic bounding-surface plasticity model for cyclic shakedown and degradation of saturated clay. *Computers and Geotechnics, 44*, 34-47.

Mroz Z, Norris V A, Zienkiewicz O C. (1978). An anisotropic hardening model for soils and its application to cyclic loading. *International Journal for Numerical and Analytical Methods in Geomechanics, 2*, 203-221.

Mroz Z, Norris V A, Zienkiewicz O C. (1979). Application of an anisotropic hardening model in the analysis of elasto-plastic deformation of soils. *Geotechnique, 29(1)*,1-34.

Prevest J H. (1977). Mathematical modeling of monotonic and cyclic undrained clay behaviour. *International Journal for Numerical and Analytical Methods in Geomechanics, 1*,195-216.

Wang J. H., Yao M. L.. (1996). Elastoplastic simulation of the cyclic undrained behavior of soft clays. *Chinese Journal of Geotechnical Engineering, 18(3)*, 11-18.

Xu GC, Xie DY, Zheng YR. (1995). Elastoplastic modeling for cyclic stress strain behavior of saturated sands. *Chinese Journal of Geotechnical Engineering, 17(2)*, 1-12.

Bazant Z P, Bhat P D. (1976). Endochronic theory of inelasticity and failure of concrete. *ASCE Journal of Engineering Mechanics Division, 102(EM4)*, 701-722.

Bazant Z P, Ansal A M, Krizek R J. (1979). Viscoplasticity of transversely isotropic clay. *ASCE Journal Engeering Mechanics Divsion, 105(4)*,549-565.

Zienkiewicz O C, Chang C T, Hinton E. (1978). Non-linear seismic response and liquefaction. *Internal Journal for Numerical and Analytical Methods in Geomechanics, 20(5)*,307-329.

Xie Dingyi, Wu Zhihui, Guo Yaotang. (1981). Application of limit equilibrium theory to the analysis of dynamic failure process of saturated sand. *China Civil Engineering Journal, 14(4)*, 17-28.

Xie Dingyih, Wu Zhihui, Guo Yaotang. (1981). The application of critical equilibrium theory to the dynamic failure process of saturated sand. *Journal of Northwest A&F University(Natural Science Edition), 1*, 1-14.

Xie Dingyi, Zhang Jianmin. (1987). Developing mechanism on transient strength deformation of saturated sand under cyclic loading. *China Civil Engineering Journal, 20(3)*, 57-70.

Dafalias Y. F. (1986). An anisotropic critical state clay plasticity model. *Mechanics Research Communications, 13*, 341-347.

Manzari M, Dafalias Y F. (1997). A critical state two-surface plasticity model for sands. *Getotechinique, 47(2)*, 255-272.

Dafalias Y F. (1986). Bounding Surface Plasticity I: Mathmatical Foundation and Hypoplasticity. *Journal of Engineering Mechanics, 112(9)*, 966-987.

Dafalias Y F, Herrmann L R. (1986). Bounding Surface Plasticity II: Application to Isotropic

Cohensive Soils. *Journal of Engineering Mechanics, 112(12)*, 1263-1291.

Dafalias Y F. (1987). Anisotropic critical state soil plasticity model. *Mechanics Research Communications, 13(6)*, 341-347.

Manzari M T, Nour M A. (1997). On implicit integration of bounding surface plasticity models. *Computers and Structures, 63(3)*, 385-392.

Ronaldo I. Borja, Chao-Hua Lin, Francisco J. Montans. (2001). Cam-Clay plasticity, Part IV: Implicit integration of anisotropic bounding surface model with nonlinear hyperelasticity and ellipsoidal loading function. *Computer Methods in Applied Mechanics and Engineering, 190*, 3293-3323.

M. ORTIZ, J. C. SIMO. (1986). An analysis of a new class of integration algorithms for elastoplastic constitutive relations. *International Journal for Numerical Methods in Engineering, 23*, 353-366.

J. C. SIMO, S. Govindjee. (1991). Nonlinear B-stability and symmetry preserving return mapping algorithm for plasticity and viscoplasticity. *International Journal for Numerical Methods in Engineering, 31*, 151-176.

J. C. SIMO. (1985). On the computational significance of the intermediate configuration and hyperelastic stress relations in finite deformation elastoplasticity. *Mechanics of Materials, 4*, 439-451.

Li Jian. (2013). On dynamic response of the red clay foundation under high-speed train loading. Institute of Rock and Soil Mechanics, Chinese Academy of Sciences.

Liang R Y, Ma F. (1992). Anisotropic plasticity model for undrained cyclic behavior of clays I: theory. *Journal of the Geotechnical Engineering, 118(2)*,229-245.

Zhou J, Sun JZ, Wu SM. (2002). Elasto-plastic model of soft clay under reversal load. Chinese *Journal of Rock and Mechanics and Engineering, 21(2)*, 210-214.

Anadarajah A, Dafalias Y F. (1986). Bounding surface plasticity III: Application to anisotropic cohesive soils. *ASCE Journal of Engineering Mechanics, 112(12)*,1292-1319.

Chen Shanxiong, Li Jian, Jiang Lingfa, etc. (2013). Improved Cam-clay model based on hyperbolic critical state and its numerical implementation. *Chinese Journal of Rock Mechanics and Engineering, 32(11)*, 2325-2333.

R. D. Krieg, D. B. Krieg. (1977). Accuracies of numerical solution methods for the elastic-perfectly plastic model. *ASME Journal of Pressure Vessel Techinology, 99*, 510-515.

H. L. Schreyer, R. F. Kulak, M. M. Kramer. (1979). Accurate numerical solutions for elastic-plastic models. *ASME Journal of Pressure Vessel Techinology, 101*, 226-234.

M. Ortiz, E. P. Popov. (1985). Accuracy and stability of integration algorithm for elastoplastic constitutive relations. *International Journal for Numerical Methods in Engineering, 21(9)*, 1561-1576.

## Appendix A

Detailed algorithm for implicit integration for the modified bounding surface model based on swell–shrink rules:

(1) Initialize

$$\triangle\varepsilon_v^{p(n+1)}=0,\triangle e_{ij}^{p(n+1)}=0,\ p_c^{(n+1)}=p_c^{(n)},L^{(n+1)}=0$$

$$M(\theta_\alpha)^{(n+1)}=\frac{1}{ap^{(n)}+b}$$

$$c^{(n+1)}=c^{(n)}=\frac{2}{3}\left[M(\theta_\alpha)^{(n)}\right]^2 p_c^{(n)}p^{(n)}/(s_{ij}^{(n)}s_{ij}^{(n)}+\frac{2}{3}\left[M(\theta_\alpha)^{(n)}\right]^2 p^{(n)}p^{(n)})$$

$$k_p^{(n+1)}=k_p^{(n)}=\left(2c^{(n)}-p_c^{(n)}/p^{(n)}\right)\left(p_c^{(n)}/p^{(n)}\right)/\left(\left(2c^{(n)}-p_c^{(n)}/p^{(n)}\right)\left(p_c^{(n)}/p^{(n)}\right)+4H_0c^{(n)}\left(c^{(n)}-1\right)\right)$$

(2) Elastic prediction

$$p^{(n+1)}=p^{(n)}+K^{(n)}\Delta\varepsilon_v^{try}$$
$$s_{ij}^{(n+1)}=s^{(n)}+2G^{(n)}\Delta e_{ij}^{try}$$
$$\overline{p}^{(n+1)}=c^{(n+1)}p^{(n+1)}$$
$$\overline{s}_{ij}^{(n+1)}=c^{(n+1)}s_{ij}^{(n+1)}$$

(3) Yield condition

$$F(\overline{p}^{(n+1)},\overline{s}_{ij}^{(n+1)},p_c^{(n+1)})<0?$$

① Yes: *F* shrinks: $p_c^{(n+1)}=\dfrac{\overline{s}_{ij}\overline{s}_{ij}}{\frac{2}{3}\left[M(\theta_\alpha)^{(n)}\right]^2\overline{p}}+\overline{p}$

Then go to (7) final stress.

② No: Conduct plastic correction.

(i) Plastic correction uses a Newton–Simpson scheme and the formula set includes:

$$f=\begin{cases} f_1=\Delta\varepsilon_v^{p(n+1)}-L^{(n+1)}\dfrac{2}{3}\left[M(\theta_\alpha)^{(n)}\right]^2\left(2c^{(n+1)}p^{(n+1)}-p_c^{(n+1)}\right) \\ f_{2\sim7}=\Delta e_{ij}^{p(n+1)}-2L^{(n+1)}c^{(n+1)}s_{ij}^{(n+1)} \\ f_8=p_c^{(n+1)}-p_c^{(n)}exp\left(\dfrac{v^{(n)}}{\lambda-\kappa}\Delta\varepsilon_v^{p(n+1)}\right) \\ f_9=c^{(n+1)}s_{ij}^{(n+1)}s_{ij}^{(n+1)}+\dfrac{2}{3}\left[M(\theta_\alpha)^{(n)}\right]^2p^{(n+1)}\left(c^{(n+1)}p^{(n+1)}-p_c^{(n+1)}\right) \\ f_{10}=p^{(n+1)}-p^{(n)}-K\left(\Delta\varepsilon_v^{\mathrm{try}(n+1)}-\Delta\varepsilon_v^{p(n+1)}\right) \\ f_{11\sim16}=s_{ij}^{(n+1)}-s_{ij}^{(n)}-2G\left(\Delta e_{ij}^{(n+1)}-\Delta e_{ij}^{p(n+1)}\right) \\ f_{17}=c^{(n+1)}+\dfrac{XY}{c^{(n)}-k_p^{(n+1)}-c^{(n)}p_c^{(n+1)}/p_c^{(n)}} \\ f_{18}=k_p^{(n+1)}-\dfrac{XZ}{XX+4H_0c^{(n+1)}\left(c^{(n+1)}-1\right)} \end{cases}$$

where, $k_p^{(n+1)}=\dfrac{\bar{K}_p}{K_p}, XY=\dfrac{c^{(n)}k_p^{(n+1)}p_c^{(n+1)}}{p_c^{(n)}}, XZ=\left(2c^{(n+1)}-p_c^{(n+1)}/p^{(n+1)}\right)p_c^{(n+1)}/p^{(n+1)}$

(ii) In the formula set,

$\left[\Delta\varepsilon_v^{p(n+1)},\Delta e_{ij}^{p(n+1)},p_c^{(n+1)},L^{(n+1)},p^{(n+1)},s_{ij}^{(n+1)},c^{(n+1)},k_p^{(n+1)}\right]$ are seen as unknowns. Therefore its Jacobi determinant (18×18 dimensional) is such that:

The elements of the first row are:

$$\frac{\partial f_1}{\partial\Delta\varepsilon_v^{p(n+1)}}=1,\frac{\partial f_1}{\partial\Delta e_{ij}^{p(n+1)}}=0,\frac{\partial f_1}{\partial p_c^{(n+1)}}=\frac{2}{3}\left[M(\theta_\alpha)\right]^2L^{(n+1)},$$

$$\frac{\partial f_1}{\partial L^{(n+1)}}=-\frac{2}{3}\left[M(\theta_\alpha)\right]^2\left(\left(2c^{(n+1)}p^{(n+1)}-p_c^{(n+1)}\right)\right),$$

$$\frac{\partial f_1}{\partial p^{(n+1)}}=-L^{(n+1)}\frac{4}{3}\left[M(\theta_\alpha)\right]^2c^{(n+1)}p^{(n+1)},$$

$$\frac{\partial f_1}{\partial s_{ij}^{(n+1)}}=0,\frac{\partial f_1}{\partial c^{(n+1)}}=-L^{(n+1)}\frac{4}{3}\left[M(\theta_\alpha)\right]^2p^{(n+1)},\frac{\partial f_1}{\partial k_p^{(n+1)}}=0$$

The elements of the second to seventh rows are:

$$\frac{\partial f_{2\sim7}}{\partial\Delta\varepsilon_v^{p(n+1)}}=0,\frac{\partial f_{2\sim7}}{\partial\Delta e_{ij}^{p(n+1)}}=1,\frac{\partial f_{2\sim7}}{\partial p_c^{(n+1)}}=0\frac{\partial f_{2\sim7}}{\partial L^{(n+1)}}=-2c^{(n+1)}s_{ij}^{(n+1)},$$

$$\frac{\partial f_{2\sim7}}{\partial p^{(n+1)}}=0,\frac{\partial f_{2\sim7}}{\partial s_{ij}^{(n+1)}}=-2L^{(n+1)}c^{(n+1)},\frac{\partial f_{2\sim7}}{\partial c^{(n+1)}}=-2L^{(n+1)}s_{ij}^{(n+1-},\frac{\partial f_{2\sim7}}{\partial k_p^{(n+1)}}=0$$

The elements of the eighth row are:

$$\frac{\partial f_8}{\partial \Delta\varepsilon_v^{p(n+1)}} = -p_c^{(n)}\frac{v^{(n)}}{\lambda-\kappa}exp\left(\frac{v^{(n)}}{\lambda-\kappa}\Delta\varepsilon_v^{p(n+1)}\right), \frac{\partial f_8}{\partial \Delta e_{ij}^{p(n+1)}} = 0, \frac{\partial 8}{\partial p_c^{(n+1)}} = 1,$$

$$\frac{\partial f_8}{\partial L^{(n+1)}} = 0, \frac{\partial f_8}{\partial p^{(n+1)}} = 0, \frac{\partial f_8}{\partial s_{ij}^{(n+1)}} = 0, \frac{\partial f_8}{\partial c^{(n+1)}} = 0, \frac{\partial f_8}{\partial k_p^{(n+1)}} = 0$$

The elements of the ninth row are:

$$\frac{\partial f_9}{\partial \Delta\varepsilon_v^{p(n+1)}} = 0, \frac{\partial f_9}{\partial \Delta e_{ij}^{p(n+1)}} = 0, \frac{\partial f_9}{\partial p_c^{(n+1)}} = -\frac{2}{3}\left[M(\theta_\alpha)\right]^2 p^{(n+1)}, \frac{\partial f_9}{\partial L^{(n+1)}} = 0,$$

$$\frac{\partial f_9}{\partial p^{(n+1)}} = \frac{2}{3}\left[M(\theta_\alpha)\right]^2\left(2c^{(n+1)}p^{(n+1)} - p_c^{(n+1)}\right), \frac{\partial f_9}{\partial s_{ij}^{(n+1)}} = 2c^{(n+1)}s_{ij}^{(n+1)},$$

$$\frac{\partial f_9}{\partial c^{(n+1)}} = s_{ij}^{(n+1)}s_{ij}^{(n+1)} + \frac{2}{3}\left[M(\theta_\alpha)\right]^2 p^{(n+1)}p^{(n+1)}, \frac{\partial f_9}{\partial k_p^{(n+1)}} = 0$$

The elements of the tenth row are:

$$\frac{\partial f_{10}}{\partial \Delta\varepsilon_v^{p(n+1)}} = K, \frac{\partial f_{10}}{\partial \Delta e_{ij}^{p(n+1)}} = 0, \frac{\partial f_{10}}{\partial p_c^{(n+1)}} = 0, \frac{\partial f_{10}}{\partial L^{(n+1)}} = 0,$$

$$\frac{\partial f_{10}}{\partial p^{(n+1)}} = 1, \frac{\partial f_{10}}{\partial s_{ij}^{(n+1)}} = 0, \frac{\partial f_{10}}{\partial c^{(n+1)}} = 0, \frac{\partial f_{10}}{\partial k_p^{(n+1)}} = 0$$

The elements of the eleventh to sixteenth rows are:

$$\frac{\partial f_{11\sim16}}{\partial \Delta\varepsilon_v^{p(n+1)}} = 0, \frac{\partial f_{11\sim16}}{\partial \Delta e_{ij}^{p(n+1)}} = 2G, \frac{\partial f_{11\sim16}}{\partial p_c^{(n+1)}} = 0, \frac{\partial f_{11\sim16}}{\partial L^{(n+1)}} = 0,$$

$$\frac{\partial f_{11\sim16}}{\partial p^{(n+1)}} = 0, \frac{\partial f_{11\sim16}}{\partial s_{ij}^{(n+1)}} = 1, \frac{\partial f_{11\sim16}}{\partial c^{(n+1)}} = 0, \frac{\partial f_{11\sim16}}{\partial k_p^{(n+1)}} = 0$$

The elements of the seventeenth row are:

$$\frac{\partial f_{17}}{\partial \Delta\varepsilon_v^{p(n+1)}} = 0, \frac{\partial f_{17}}{\partial \Delta e_{ij}^{p(n+1)}} = 0, \frac{\partial f_{17}}{\partial p_c^{(n+1)}} = \frac{YZ}{\left(c^{(n+1)} - k_p^{(n+1)} - c^{(n+1)}p_c^{(n+1)} / p_c^{(n)}\right)^2}, \frac{\partial f_{17}}{\partial L^{(n+1)}} = 0,$$

$$\frac{\partial f_{17}}{\partial p^{(n+1)}} = 0, \frac{\partial f_{17}}{\partial s_{ij}^{(n+1)}} = 0, \frac{\partial f_{17}}{\partial c^{(n+1)}} = 1, \frac{\partial f_{17}}{\partial k_p^{(n+1)}} = \frac{ZY}{\left(c^{(n)} - k_p^{(n+1)} - c^{(n)}p_c^{(n+1)} / p_c^{(n)}\right)^2}$$

The elements of the eighteenth row are:

$$\frac{\partial f_{18}}{\partial \Delta\varepsilon_v^{p(n+1)}} = 0, \frac{\partial f_{18}}{\partial \Delta e_{ij}^{p(n+1)}} = 0, \frac{\partial f_{18}}{\partial p_c^{(n+1)}} = \frac{-XX*ZZ - ZX*ZZ}{XX^2},$$

$$\frac{\partial f_{18}}{\partial L^{(n+1)}} = 0, \frac{\partial f_{18}}{\partial p^{(n+1)}} = \frac{-XX*YY - ZX*YY}{XX^2}, \frac{\partial f_{18}}{\partial s_{ij}^{(n+1)}} = 0,$$

$$\frac{\partial f_{18}}{\partial c^{(n+1)}} = \frac{-2XX*p_c^{(n+1)} / p^{(n+1)} - ZX*\left(2p_c^{(n+1)} / p^{(n+1)} + 8H_0c^{(n+1)} - 4H_0\right)}{XX^2}, \frac{\partial f_{18}}{\partial k_p^{(n+1)}} = 1$$

where,

$$XX = \left(2c^{(n+1)} - p_c^{(n+1)} / p^{(n+1)}\right) p_c^{(n+1)} / p^{(n+1)}$$

$$YY = -2c^{(n+1)} p_c^{(n+1)} / \left(p^{(n+1)} p^{(n+1)}\right) + 2p_c^{(n+1)} / \left(p^{(n+1)} p^{(n+1)} p^{(n+1)}\right)$$

$$ZZ = 2c^{(n+1)} / p^{(n+1)} - 2p_c^{(n+1)} / \left(p^{(n+1)} p^{(n+1)}\right)$$

$$YZ = \left(c^{(n)} - k_p^{(n+1)} - c^{(n)} p_c^{(n+1)} / p^{(n+1)}\right)\left(c^{(n)} k_p^{(n+1)} / p_c^{(n)}\right) + c^{(n)} c^{(n)} k_p^{(n+1)} p_c^{(n+1)} / \left(p_c^{(n)} p_c^{(n)}\right)$$

$$ZY = \left(c^{(n)} - k_p^{(n+1)} - c^{(n)} p_c^{(n+1)} / p^{(n+1)}\right)\left(c^{(n)} k_p^{(n+1)} / p_c^{(n)}\right) + c^{(n)} k_p^{(n+1)} p_c^{(n+1)} / p_c^{(n)}$$

$$ZX = \left(2c^{(n+1)} - p_c^{(n+1)} / p^{(n+1)}\right) p_c^{(n+1)} / p^{(n+1)}$$

(iii) Set an initial vector:

$$x^0 = \left\{\Delta\varepsilon_v^{p(n+1)}, \Delta e_{ij}^{p(n+1)}, p_c^{(n+1)}, L^{(n+1)}, p^{(n+1)}, s_{ij}^{(n+1)}, c^{(n+1)}, k_p^{(n+1)}\right\}$$

$$= \left\{0, 0, p_c^{(n)}, 0, p^{try}, s_{ij}^{try}, c^{(n)}, k_p^{(n)}\right\}$$

Set a residual error vector:

$\boldsymbol{f} = \{f_1, f_2, f_3, f_4, f_5, f_6, f_7, f_8, f_9, f_{10}, f_{11}, f_{12}, f_{13}, f_{14}, f_{15}, f_{16}, f_{17}, f_{18}\}$

(iv) Calculate $\|\boldsymbol{f}\|$

(a) If $\|\boldsymbol{f}\| \leqslant$ TOL, exit iteration.

(b) If $\|\boldsymbol{f}\| >$ TOL, continue iteration until $\|\boldsymbol{f}\| \leqslant$ TOL.

(4) Parameters and stress update

$$\sigma_{ij}^{(n+1)} = s_{ij}^{(n+1)} + p^{(n+1)}\delta_{ij}$$

$$v^{(n+1)} = v^{(n)}\left(1 - \Delta\varepsilon_v^{(n+1)}\right)$$

$$K^{(n+1)} = \frac{v^{(n+1)}}{\kappa} p^{(n+1)}$$

$$G^{(n+1)} = \frac{3(1-2\mu)}{2(1+\mu)} K^{(n+1)}$$

**Appendix B**

All symbols and their meanings as used in this paper are listed in the following table.

Symbols table

| | | | |
|---|---|---|---|
| $\sigma_{ij}$ | stress tensor | $\theta_\alpha$ | Lode angle |
| $\bar{\sigma}_{ij}$ | stress tensor on bounding surface | $a$ | parameter of hyperbolic critical line |
| $p$ | volumetric stress | $b$ | parameter of hyperbolic critical line |
| $\bar{p}$ | volumetric stress on bounding surface | $K_p$ | plastic modulus |
| $s_{ij}$ | deviatoric stress | $\bar{K}_p$ | plastic modulus corresponding to the bounding surface equation |
| $\bar{s}_{ij}$ | deviatoric stress on bounding surface | $k_p$ | $\bar{K}_p / K_p$ |
| $\varepsilon_{ij}$ | strain tensor | $H_0$ | parameter of the constitutive model |
| $\varepsilon_v$ | volumetric strain | $M(\theta_\alpha)$ | slope of the critical line |
| $e_{ij}$ | deviatoric strain | $L$ | plastic loading index |
| $\varepsilon_{ij}^p$ | plastic strain tensor | $E$ | elastic modulus tensor |
| $\varepsilon_v^p$ | plastic volumetric strain | $K$ | volumetric modulus |
| $e_{ij}^p$ | plastic deviatoric strain | $G$ | shear modulus |
| $v$ | specific volume | $J_2$ | second deviatoric stress invariant |
| $\lambda$ | slope of normal consolidation line | $J_3$ | third deviatoric stress invariant |
| $\kappa$ | slope of elastic swelling line | $\delta_0$ | distance between the mapping origin and the virtual stress |
| $p_c$ | hardening parameter | $\delta$ | distance between the mapping origin and the real stress |
| $M_e$ | slope of tensile critical line | $c$ | $\delta_0/(\delta_0-\delta)$ |
| $M_c$ | slope of compressive critical line | $F$ | bounding surface |